catalysts

MDPI

Article

Aqueous-Phase Glycerol Conversion over Ni-Based Catalysts Synthesized by Nanocasting

Adriana Morales-Marín [1], Unai Iriarte-Velasco [2], Miguel Ángel Gutiérrez-Ortiz [1] and Jose Luis Ayastuy [1,*]

[1] Department of Chemical Engineering, Faculty of Science and Technology, University of the Basque Country (UPV/EHU), 48940 Leioa, Spain; adriana.morales@ehu.eus (A.M.-M.); miguelangel.gutierrez@ehu.eus (M.Á.G.-O.)
[2] Department of Chemical Engineering, Faculty of Pharmacy, University of the Basque Country (UPV/EHU), 01006 Vitoria-Gasteiz, Spain; unai.iriarte@ehu.eus
* Correspondence: joseluis.ayastuy@ehu.eus

Abstract: A morphological strategy consisting of nanocasting synthesis of nickel aluminate spinel precursor was addressed. Two nanocasted catalysts were synthesized involving different template-removal procedures (i.e., Teflon-assisted calcination vs. NaOH washing) for spinel recovery. As a reference, spinel $NiAl_2O_4$ supported by SBA-15 and bare nickel aluminate spinel were selected. The obtained solids were characterized in detail, examining their textural, acid–base, structural and compositional characteristics, either in the calcined or reduced forms. The as-obtained catalysts' performance was evaluated in the aqueous-phase reforming of glycerol at 235 °C and 35 bar. Exhausted samples were also characterized to enlighten changes in catalyst properties during the aqueous-phase reaction. NiAl/SBA-15 and NiAl-NCF catalyst showed very poor catalytic performance for the glycerol transformation. NiAl-NCN catalyst presented improved activity with respect to NiAl, with a 20% higher hydrogen production rate but, as a drawback, higher methane formation for a whole range of glycerol conversions. Exhausted catalyst indicated nickel oxidized in liquid phase reaction.

Keywords: nickel; spinel; nanocasting; SBA-15; glycerol; aqueous phase; hydrogen

Citation: Morales-Marín, A.; Iriarte-Velasco, U.; Gutiérrez-Ortiz, M.Á.; Ayastuy, J.L. Aqueous-Phase Glycerol Conversion over Ni-Based Catalysts Synthesized by Nanocasting. *Catalysts* **2022**, *12*, 668. https://doi.org/10.3390/catal12060668

Academic Editors: Charles Xu and Tianliang Lu

Received: 27 May 2022
Accepted: 15 June 2022
Published: 18 June 2022

1. Introduction

In the most recent decade, the climate system has undergone various changes in the atmosphere, biosphere, cryosphere, and oceans, which evidence the climate emergency [1]. In the 2011–2020 period, the global mean surface temperature has increased on average by 1.09 °C (0.95–1.20 °C). The amount of energy that Earth's oceans have adsorbed increased by 10^{24} joule between 1971 and 2018, and in response, the global mean sea level rose by 0.20 m by 2018. Snow cover decreased, and the shrinking of glaciers has led to the lowest total glacier mass. The annual land area mean precipitation in the Northern Hemisphere temperate regions has increased, while it decreased in the sub-tropical dry regions. In addition, severe wildfires and the resulting deforestation have also increased [2]. The substantial increase in anthropogenic Green House Gas (GHG) emissions to 52 $GtCO_2$-eq/yr has boosted global warming [3]. Being the energy sector the main source (around three-quarters), thus it holds the key to the goal of limiting global warming to less than 2 °C by 2050, as signed in the Paris Climate Agreement (2015) [4]. In this line, the future transformation of the energy sector could connect climate change mitigation challenges with social development and equity.

This work is driven to contribute to this matter, specifically to seek possible synergies between biofuels and renewable hydrogen production chains by producing H_2-rich streams from bioglycerol. Currently, most fuels and chemicals are produced from fossil raw materials with the resulting environmental problems. The use of biomass is one alternative for sustainable development.

Glycerol, an abundant by-product of biodiesel, is considered one of the platform molecules derived from biomass that can be transformed into high-value-added products. A stable crude glycerol generation is expected in the near future [5], ensuring its availability as feedstock for conversion processes.

Glycerol can be converted into H_2 or chemicals by means of energetically advantageous conversion in the aqueous phase [6]. The H_2 production by the aqueous-phase reforming (APR) of glycerol allows the valorization of biorefinery waste streams without employing fossil sources. APR process, first reported in the early 2000s, consists of a one-step catalytic process, which operates at low temperatures (150–270 °C) and pressures high enough to keep the reactants in the liquid phase (usually 15–60 bar) [7]. Therefore, it avoids the energetically intensive steam generation step necessary in steam reforming (SR) [8]. Waste aqueous streams from lignocellulosic biomass treatments [9], food industry [10], petrochemicals [11], or biodiesel industry [12] can be processed by APR to convert oxygenated molecules into valuable products [13]. For glycerol, the complete reforming ideally yields seven moles of H_2, and three moles of CO_2, per mole of glycerol that reacts, as shown in Equation (1).

$$C_3H_8O_3\ (l) + 3\,H_2O\ (l)\ \rightarrow\ 3\,CO_2 + 7\,H_2 \quad (1)$$

The reforming reaction mechanism consists of many reactions, but it can be described as the sum of two consecutive steps: decomposition of glycerol by C-C bond cleavage and subsequent WGS. However, undesired side reactions must be taken into account in the global process, including hydrogenation of CO and CO_2, along with Fisher–Tropsch and dehydration, among others [6].

The low temperature of the APR enhances the Water–Gas Shift (WGS) reaction (chemical equilibrium) and enables low-CO streams. These streams can be directly fed to the fuel cell to produce power, heat, or gas fuel [14]. At the same time, the high pressure employed makes the produced gaseous stream more suitable for in situ CO_2 capture and sequestration by Pressure Swing Adsorption or membrane technologies [15].

A proper catalyst formulation for APR should ideally provide high reaction rates under optimal operating conditions, high selectivity to H_2, and resistance against deactivation, and should avoid the use of noble metals for economic purposes. Moreover, the catalyst must be effective in breaking the C-C, O-H, and C-H bonds. In addition, the catalyst should promote the WGS reaction of adsorbed CO since it prevents catalyst poisoning and avoids hydrogenation reactions of CO and/or CO_2 to form alkanes via methanation and FT reactions [15]. The choice of the active metal, the possible promoters, and the type of the support are critical for the APR performance since they can strongly affect the active phase dispersion, environment, acidity, etc. [16,17].

Platinum is the most studied metal for APR since it combines high activity and moderate selectivity [15]. Provided its much lower cost and comparability to noble metal catalytic performance, Ni is a promising metal for APR applications, either as a monometallic [18] or bimetallic catalytic system [19]. In previous work, we reported a nickel catalyst derived from nickel aluminate spinel precursor as very active for H_2 production [18]. Other requirements for the catalyst are related to a high specific surface area, smaller crystals (high dispersion), and hydrothermal and chemical stability [16].

This paper addresses the synthesis of a nickel aluminate by nanocasting for the glycerol AP conversion, using SBA-15 as a hard template. This strategy could lead to a nanostructured nickel aluminate with improved accessibility and stability properties, which are particularly desirable for processes that take place at the solid-liquid interphase [20]. Indeed, nanocasted catalysts can enhance the transport and diffusion of the reactants and products, providing a shorter diffusion pathway and a higher surface/volume ratio [21].

The catalytic performance, in terms of H_2 production, can be improved by using nanocasted catalysts. However, structured Ni catalysts have been mostly tested in gas-phase reactions. For instance, nanostructured Ni-based spinel showed high activity and stability in the dry methane reforming for hydrogen production [22,23]. Steam-reforming

(SR)-supported Ni/SBA-15 catalysts achieved high CH_4 conversion for the combined steam methane reforming (SMR) and Water–Gas Shift (WGS) reaction [24]. Furthermore, bimetallic Ni-(Cu, Co, Cr)/SBA-15, with small Ni crystallites, showed a good performance in the glycerol SR [25]. The number of works focused on the aqueous-phase reaction by supported ordered mesoporous catalysts is scarce [26]. Moreover, to the best of our knowledge, the nanocasting of mixed oxides for the aqueous-phase conversion of glycerol has not been reported yet.

Here, a nickel aluminate spinel supported over SBA-15 is prepared. The removal of the SBA-15 template is by two methods, i.e., by leaching with NaOH and by Teflon-assisted calcination. The later procedure avoids using toxic HF since the silica framework can be removed through the formation of SiF_4 [21]. As a reference, bare nickel aluminate spinel has also been synthesized. The prepared catalysts have been investigated in the liquid-phase glycerol conversion, and the catalytic results are correlated with the intrinsic characteristics of the catalysts.

2. Results

2.1. Catalysts Characterization

2.1.1. Surface Characteristics

The bulk chemical composition of the solids is reported in Table 1. The Ni/Al molar ratio of NiAl/SBA-15 was 0.6, which is higher than the stoichiometric value (0.5), suggesting that nickel salt was better diffused into the silica pores. Indeed, the synthesis of bimetallic oxides supported on the SBA-15 template is challenging, especially the control over the resultant chemical composition and phases [27,28]. Ni/Al ratio notably changed after template removal. On the one hand, the Ni/Al ratio in NaOH-etched NiAl-NCN catalyst increased by 17% (up to 0.74), associated with the leaching of aluminum. It is known that aluminum can form water-soluble sodium aluminate in basic media, which would promote Al leaching [29]. On the other hand, the bulk Ni/Al ratio of NiAl-NCF (0.48) remained close to the stoichiometric value. In general, ICP results revealed a massive removal of Si from the hard template in both NiAl-NCN and NiAl-NCF replicates, even though some residual silica (<3%) remained. NaOH etching was more efficient than calcination with Teflon for silica removal. It seemed that SBA-15 could hinder the formation of the $NiAl_2O_4$ phase during the calcination. As previously noted, the loss of active metals during the template removal, caused the imbalance of Ni/Al stoichiometric proportion.

The N_2 adsorption-desorption isotherms and the pore size distribution of the calcined and reduced forms of the solids are shown in Figure 1. All the solids exhibited type IV isotherms (IUPAC classification) with an H1 hysteresis loop (condensation and evaporation steps characteristic of periodic mesoporous materials). There are no substantial differences among the isotherms for calcined and reduced forms of the solids, which indicated that porous structure was maintained upon reduction. The narrow range of P/P_0 of the hysteresis from SBA-15 was consistent with the presence of tubular pores of uniform size [30]. The bimodal pore size distribution in the NiAl/SBA-15 composite could be ascribed to the partial blockage of template pores by the newly formed oxide. BET surface area (S_{BET}) of the calcined and reduced forms (reduced at 700 °C, 1 h) of the solids are shown in Table 1. SBA-15 material prepared by hydrothermal synthesis and calcination at 850 °C showed an S_{BET} of 459 m^2/g, an average pore diameter of 5.5 nm, and a pore volume of 0.76 cm^3/g. Both S_{BET} and V_{pore} of NiAl/SBA-15 assay decreased by around 60%, indicating pore filling by the oxides. The template removal method was affected differently on the S_{BET}. NiAl-NCF showed a severe pore collapse (S_{BET} decreased by 62% with respect to NiAl/SBA-15), with a notable increase in the average pore diameter (22.1 nm), likely due to the collapse of small pores. On the contrary, NaOH-etched NiAl-NCN assay increased its S_{BET} by 46% with respect to parent NiAl/SBA-15 (210 vs. 306 m^2/g). These assays showed similar pore volume and average pore width, suggesting the formation of a wormhole-like rod structure after removal of the siliceous template. According to [26], the incomplete filling of the

pores during the impregnation step could form such a pore structure. It is noticeable that NiAl/NCN assay had 3-fold higher S_{BET} than the reference NiAl (306 vs. 98 m^2/g).

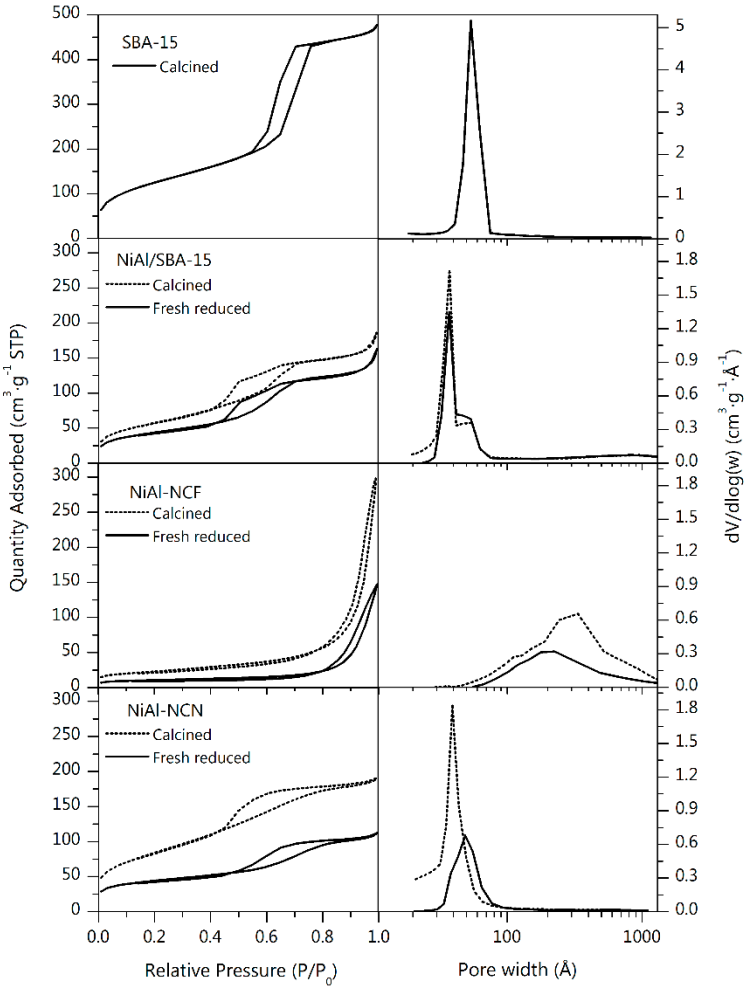

Figure 1. N_2 adsorption−desorption isotherms and pore size distributions in the calcined and reduced forms of catalysts.

Table 1. Bulk chemical composition, textural and acid/base properties and crystallite sizes of Ni^0 and exposed metallic surface.

Solid	Ni/Al (at./at.)	Si [a] (%)	S_{BET} (m^2/g)	V_{pore} (m^3/g)	d_{pore} (nm)	Acid/Base Ratio [b] (mol_{NH3}/mol_{CO2})	d_{Ni^0} -XRD (nm)	d_{Ni^0} -TEM (nm)	D_{Ni^0} [c] (%)	A_{Ni^0} [d] (m^2_{Ni} /g)
NiAl	0.49	n.a.	98 (83)	0.27 (0.29)	8.4 (10.8)	1.7	16.0	12.0	10.0	14.1
NiAl/SBA-15	0.60	55.8	210 (158)	0.30 (0.26)	4.7 (5.5)	7.2	24.3	25.8	3.6	7.3
NiAl-NCN	0.74	1.2	306 (155)	0.33 (0.15)	3.9 (5.4)	2.7	6.7	9.0	12.0	17.9
NiAl-NCF	0.48	2.9	81 (38)	0.46 (0.22)	22.1 (20.9)	15.7	27.7	31.7	3.2	3.8

Values in parenthesis: reduced solids; [a]: wt.%; [b] in reduced form; [c] dispersion; [d] surface area.

After reduction, S_{BET} decreased for all solids (i.e., 15–53%). The reference NiAl solid showed the highest textural stability to reduction treatment (i.e., 15% decrease). Nonetheless, NiAl/SBA-15 and NiAl-NCN still showed a higher S_{BET} than that of NiAl. Again, NiAl-NCF showed a less porous surface.

Aqueous-phase reforming of glycerol involves, among others, dehydration reactions [31], which are very sensitive to the catalyst's surface acid–base properties [32]. Indeed, Pt- catalysts are more affected by acidity and the Pt domain size [33]. Basic surfaces are known to enhance H_2 selectivity via WGS promotion (a key step in APR, where CO is

converted with additional production of H_2) [34]. Acid surfaces, on the contrary, promote dehydration, giving rise to hydrogen-consuming liquid intermediates [33], thus promoting the production of alkanes and HDO products. The acid and basic site density were calculated from NH_3-TPD and CO_2-TPD, respectively. Table 1 shows the acid/base site ratio of the reduced forms of solids. Reference NiAl assay showed amphoteric characteristics since the acid/base ratio was 1.7. When NiAl was supported onto the siliceous template, the ratio increased by 4 (up to 7.2). Interestingly, among the nanocasted solids, NiAl-NCN decreased the acid/basic sites ratio with respect to its parent solid (2.7 vs. 7.2) while NiAl-NCF solid increased by two-fold (15.7). The amphoteric nature of the alumina affected the acidity of the solids more significantly than SiO_2 did.

2.1.2. Morphological and Structural Characteristics

The template SBA-15 calcined at 850 °C showed characteristic Si-O transmittance bands and O-H stretching bands in its FTIR spectrum (Figure S1, Supplementary Materials). A wide, intense peak at 3600–3000 cm^{-1} and a peak at around 1620 cm^{-1} was associated with the O-H bending of the silanol group and stretching vibration mode of the water in the interlayer spaces, respectively [35]. The strong band in the 1200–920 cm^{-1} region was due to the asymmetric stretching mode of Si-O-Si.

Low angle XRD diffractograms of the SBA-15 template and NiAl/SBA-15 composite are shown in Figure 2. The 2-D hexagonal (*p6mm*) mesoporous structure of the SBA-15 was confirmed by the diffraction peaks at 1.1°, 1.8°, and 2.1° (2θ) [36].

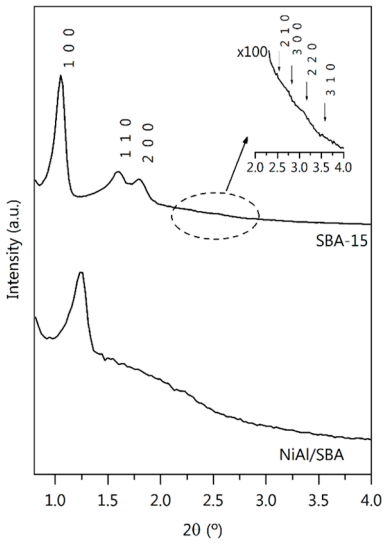

Solid	$d_{(100)}$ (nm)	a_0 (nm)	W_t (nm)
SBA-15	7.9	9.1	3.6
NiAl/SBA-15	7.1	8.2	3.5

Figure 2. Low-angle XRD diffractogram for calcined forms of SBA-15 and NiAl/SBA-15. In the table, d-spacing, lattice parameter and wall thickness.

The intense (1 0 0) peak and the corresponding unit cell spacing obtained indicated a large unit-cell parameter of the template (9.1 nm). The pore wall thickness of 3.6 nm was estimated by subtracting the average pore diameter from the unit cell spacing. It is worth noting that, despite being calcined at a temperature as high as 850 °C, the obtained SBA-15 presented high structural stability, as evidenced by the presence of the peak (1 0 0) peak. The (1 0 0) plane of NiAl/SBA-15 composite upshifted by around 2 = 1.25°, which reflected a smaller unit cell spacing (8.2 nm). The very low intensity of (1 1 0) and (2 0 0) X-ray diffraction peaks for this solid suggested a less-organized pore structure, which could be due to the presence of nickel and aluminum-containing species in the porous system. The wall thickness for NiAl/SBA-15 was almost the same as the SBA-15 template (3.5 nm). The low-angle XRD patterns for both nanocasted samples, much weaker, are also included in the inset of Figure 3A. On the one hand, NiAl-NCN presented a peak at small angles corresponding with the 2-D structure (1 0 0), suggesting a wormhole-like rod structure

replica of the SBA-15 template after NaOH etching. The broadness and not well resolved *p6mm* reflections indicated hollow framework interference with the diffraction lines [26]. On the other hand, the low-angle diffractogram of NiAl-NCF seemed smooth, which could be due to a structural deterioration owing to the Teflon-assisted calcination.

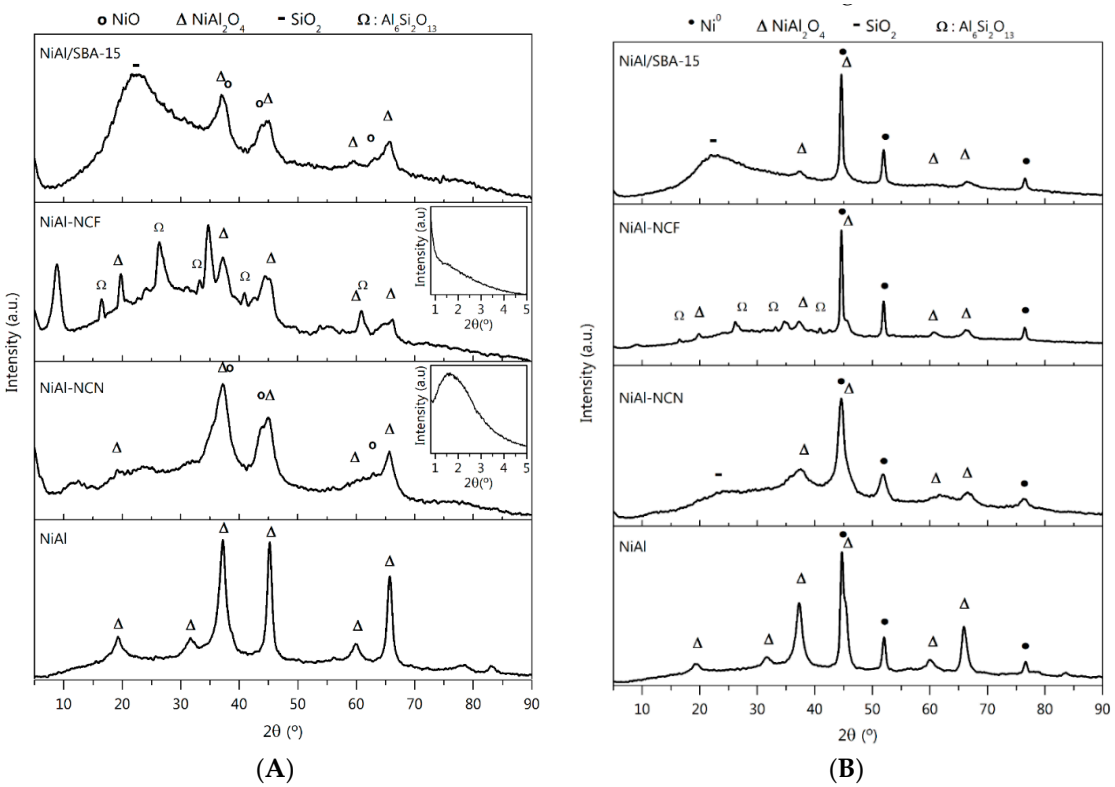

Figure 3. XRD diffractograms for the (**A**) calcined and (**B**) reduced forms of the solids. Insets include small-angle RXD patterns.

Wide-angle XRD diffractograms for all calcined solids are shown in Figure 3A. A large bump indicating the presence of amorphous silica was noticed for all solids except NiAl. Moreover, XRD of all solids showed features of cubic $NiAl_2O_4$ spinel phase (JCPDS 78-1601). In the case of the NiAl/SBA-15 solid, characteristic diffraction peaks of NiO were also observed (JCPDS 01-78-0643). Due to the larger than stoichiometric Ni/Al ratio in this sample, the excess of Ni was segregated as NiO, resulting in an XRD signal [37]. Among nanocasted solids, only NiAl-NCN contained NiO phase, in accordance with its higher than stoichiometric Ni/Al ratio. Concomitantly, the lower than stoichiometric ratio of NiAl-NCF solid would explain the absence of NiO peaks in its diffractogram. In the later solid, the spinel characteristic features were slightly upshifted, suggesting the spinel was enriched in alumina (nickel-defective spinel phase). In addition, peaks from the mullite phase ($Al_6Si_2O_{13}$) were detected (JCPDS 015-0776). Other diffraction signals (at 8.72, 34.7, 42, 44.3, 64.1° 2θ), probably due to new species formed during the calcination with Teflon, could not be identified.

Upon reduction, diffraction peaks related to metallic nickel were visible for all samples at 45, 52, and 77° 2θ positions (JCPDS 01-078-0712). Furthermore, for all the solids, peaks from the spinel phase remained, which suggested that the employed reduction temperature (700 °C) was not high enough to exudate all the Ni^0 from the spinel framework.

The values of the average metallic nickel domain size ($d_{Ni^0\text{-XRD}}$), calculated from the X-ray broadening, are summarized in Table 1. Notably, metallic nickel crystallites in NiAl/SBA-15 solid were larger than the unit-cell parameter of the template (24.3 vs. 9.1 nm), suggesting that part of nickel was deposited in the external surface of the template. Among the nanocasted solids, NiAl-NCN presented the smallest average size of Ni^0

crystals (6.7 nm). On the contrary, very big metallic nickel domains were observed for the NiAl-NCF solid.

To further investigate the catalyst morphology and particle size, TEM analysis was carried out (Figure 4). In its calcined form, the synthesized SBA-15 template evidenced an ordered mesoporous network with long-parallel channels of pores. The image analysis (ImageJ software) allowed us to measure the channel pore size (4.5 nm), which was close to that estimated from the N_2 physisorption (d_{pore} = 5.5 nm). Moreover, the distance between the channel walls was 9.2 nm, in good agreement with the unit cell spacing estimated from XRD. In NiAl/SBA-15 composite, NiAl particles were observed either in the inner part of the channels or outside of them.

After template removal, TEM micrographs of NiAl-NCF and NiAl-NCN calcined samples displayed particles of homogeneous morphology and similar sizes that were closer to each other. A wormhole-like rod structure was evidenced for both solids, as also detected by nitrogen isotherms and low-angle XRD. The most notable difference between nanocasted solids and reference NiAl was less uniform morphology, lower particle density, and less ordering of the latter.

For fresh reduced NiAl/SBA-15 assay, near-spherical particles were found of very different sizes, ranging from 5 to above 50 nm (average 25.8 nm), which agreed with the NiAl distribution in the channels and outside of the template. The nanocasted solids showed nearly spherical-shaped metallic Ni particles that could be observed for NiAl-NCN solid, with a homogeneous and ordered appearance. Contrarily, NiAl-NCF catalyst contained agglomerates of Ni^0 particles of different shapes. For example, cubic agglomerated Ni^0 particles could be observed for this solid. For NiAl-NCN solid, the Ni^0 particles had unimodal size distribution, with a maximum at about 9 nm, which was smaller than that of reference NiAl (12 nm). Calcination with Teflon led to a wide particle size distribution (particles in the 11 to 50 nm range) with an average particle size of 31.7 nm, much larger than that of reference NiAl. The formation of hot spots in the calcination with Teflon could promote the coalescence of nickel particles.

Among the nanocasted solids, NiAl-NCN solid presented the highest Ni^0 surface area (Table 1), even higher than that of reference NiAl (17.9 vs 14.1 $m^2{}_{Ni}{}^0/g$); therefore, it had the highest nickel dispersion (12%). On the contrary, NiAl-NCF showed a very low metallic area, in agreement with its larger Ni^0 particle size, which limited metal dispersion (4-fold lower than that of NiAl-NCN). Their precursor NiAl/SBA-15 showed low dispersion and metallic area, suggesting that most of the NiAl particles were deposited on the template surface. Based on the TEM micrographs, it could be concluded that the nanocasted solid's morphology was highly influenced by the template removal procedure. It could be seen that NaOH etching enhanced the nickel dispersion, while the Teflon-assisted removal approach yielded a catalyst with a less accessible Ni^0 surface. The existence of other nickel-containing phases not detected by XRD cannot be discarded.

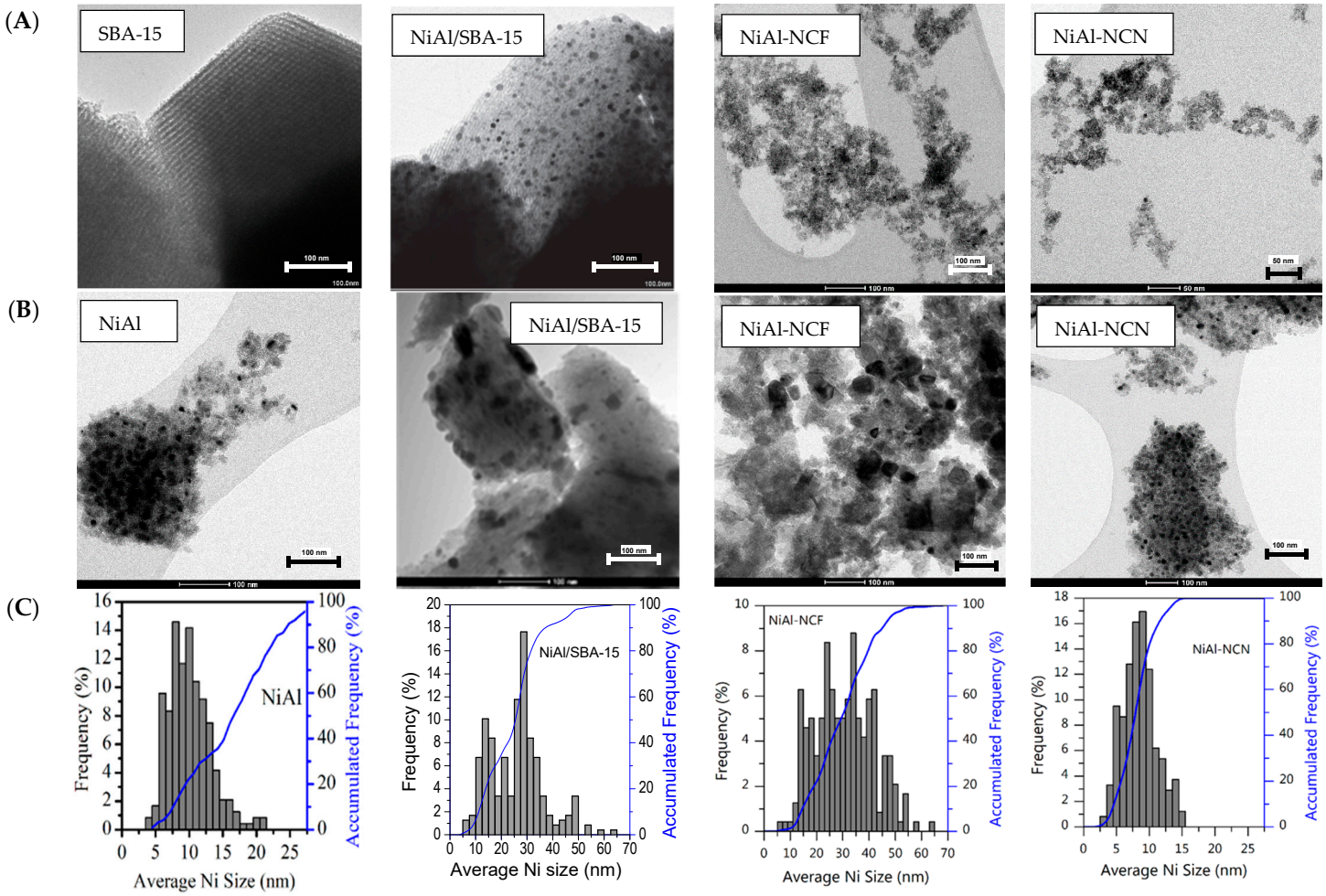

Figure 4. TEM images for (**A**) calcined and (**B**) fresh reduced forms of the solids. (**C**) Ni^0 particle size distributions.

2.1.3. Reducibility and Speciation Analysis

The reducibility of the solids was analyzed by H_2-TPR. The reduction profiles, up to 950 °C (TPR_{950}), of the calcined solids are shown in Figure 5. The obtained profiles, with a long left tail, indicated nickel species of different reducibility. Similar to parent NiAl, all calcined solids presented peaks in three temperature zones, namely α, β and γ, which are related to the H_2 consumption at low, medium, and high temperatures, respectively. The peak assignment was as follows [18,38]: peak-α (free NiO particles at the surface), peak-β (nickel in sub-stoichiometric spinel $Ni_{1-X}Al_2O_{4-X}$), and peak-γ (nickel in stoichiometric spinel $NiAl_2O_4$). Peak-β was split into two contributions: β1 (at a lower temperature) and β2 (at a higher temperature), referred to as Ni-rich and Ni-lean $Ni_{1-X}Al_2O_{4-X}$ solid, respectively [18].

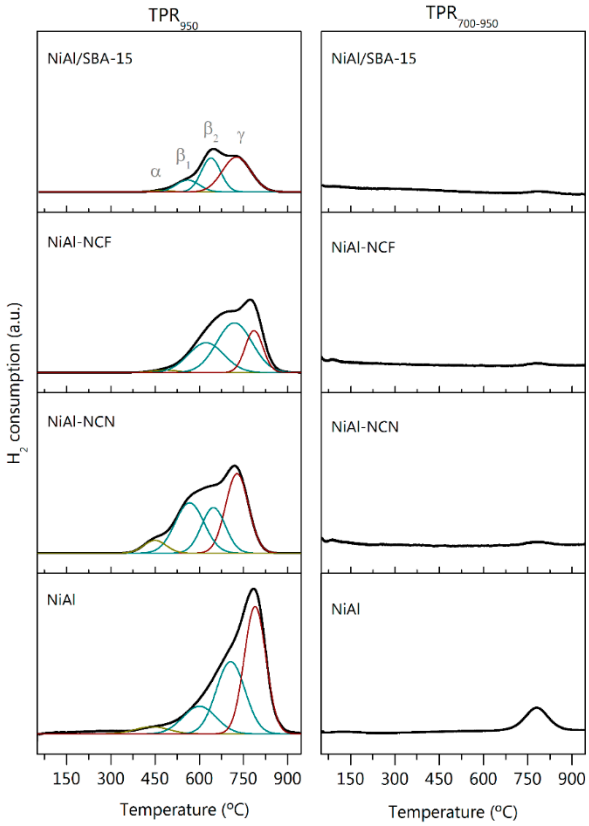

Figure 5. H_2-TPR profiles of NiAl/SBA-15 and nanocasted solids. TPR_{950}: reduction profile of calcined solids; $TPR_{700–950}$: reduction profile of fresh reduced catalyst.

For the reference NiAl catalyst, the peak-α was centered at around 450 °C, peak-β at around 600 and 685 °C, and peak-γ at around 790 °C. The H_2 consumption in the 550–740 °C range could also involve the contribution of Ni^{2+} species interacting with silica [24], as suggested by the XRD data.

The hydrogen consumption in TPR_{950} is reported in Table 2. It is remarkable the similarity to theoretical hydrogen uptake (within the experimental error) for NiAl and NiAl/SBA-15 solids. It was related to a complete reduction of Ni species in those calcined solids. However, for both nanocasted solids, about 20% lower than theoretical hydrogen consumption was measured. The existence of hardly reducible Ni^{2+} species (for instance, mullite, as observed by XRD) could explain such a difference. For reference, NiAl solid, free NiO (α-peak), accounted for 1.5% of the total Ni loaded, while β-type nickel accounted for 53.8%. A similar distribution of α and γ Ni^{2+} species remained for the composite solid, with a little trade-off between β1 and β2 contributions. For the nanocasted NiAl-NCF solid, the contribution of α-type nickel was similar to its parent solid (1.6%); however, γ-peak contribution fell by half, with the concomitant increase in β-type contribution (77.7% vs.

47.8%). The nanocasted NiAl-NCN solid showed an increased amount of α-type nickel species whereas γ-peak slightly decreased as compared to its parent solid. Indeed, this solid had the largest contribution of α-type nickel among all (6.2%). Both nanocasted solids presented a higher proportion of β-type nickel species than their parent solid NiAl/SBA-15. It is known that free NiO offers poor nickel anchoring, leading to bigger Ni^0 particles upon reduction [39]. Therefore, it was expected that NiAl-NCN, the one with the highest contribution of α-type nickel species, had the biggest Ni^0 entities. However, it had the smallest ones (around 30 nm, Table 1), suggesting that the growth of the crystal was controlled by the SBA-15 framework.

Table 2. Results of H_2-TPR for NiAl/SBA-15 and nanocasted solids.

Catalyst	Calcined					Fresh Reduced		
	TPR_{950} H_2-Uptake (mmol H_2/g)	Nickel Speciation (%)				$TPR_{700–950}$ H_2-Uptake (mmol H_2/g)	DR_{Ni} [(1)] (%)	Ni^0 Content (mmol H_2/g)
		α	β_1	β_2	γ			
NiAl	5.6 (5.6)	1.5	21.3	23.4	53.8	0.56	79	4.4
NiAl/SBA-15	2.0 (2.1)	1.7	14.2	33.6	50.6	0.22	88	1.8
NiAl-NCN	5.2 (6.7)	6.2	31.4	23.3	39.1	0.16	97	5.0
NiAl-NCF	4.0 (5.0)	1.6	29.1	48.6	20.6	0.10	98	3.9

In parenthesis, the theoretical uptake; [(1)] Degree of Reduction.

Prior to the catalytic runs, the catalysts were reduced at 700 °C for 1 h. In order to measure the reduction degree of Ni (DR_{Ni}) and the amount of metallic Ni exuded from the spinel lattice, the so-called $TPR_{700–950}$ procedure was used, which consisted of a TPR analysis for a solid reduced at 700 °C for 1 h. The obtained $TPR_{700–950}$ profiles are shown in Figure 5. The obtained profiles consisted of weak reduction peaks at temperatures above 700 °C, which indicated that after the reduction treatment, a fraction of nickel remained in the stoichiometric spinel phase, i.e., as γ-type nickel. The degree of reduction of nickel (DR_{Ni}), calculated as the percentage of hydrogen uptake in TPR_{700} with respect to that in TPR_{950}, decreased as follows: NiAl-NCF > NiAl-NCN > NiAl/SBA > NiAl (see Table 2). It was evidenced that nickel reducibility was promoted in the composite and nanocasted catalysts.

2.2. Catalytic Performance Tests

A priori, advantageous physicochemical characteristics were found for catalysts synthesized by nanocasting methodology, especially for NiAl-NCN. Superior BET area, some mesostructured order, and high reducibility were, in general, the improved physicochemical characteristics of this sample. Moreover, controlled growth of Ni^0 crystallites was found in the solids that presented structural ordering. The effect of those characteristics on the glycerol APR is discussed in this section.

The catalytic performance of the catalysts in the aqueous-phase transformation of glycerol was evaluated in a tubular reactor. Reaction indices shown were obtained at TOS = 3 h. It must be noted that reaction indices remained constant during the 3 h run (Figure S2, Supplementary Materials). In order to ensure that experiments were performed in a kinetic regime, i.e., in the absence of mass transfer limitations, the Weisz–Prater (Φ_{WP}) and Mears criteria (MR) were applied for the internal and external mass transfer limitations, respectively. The fastest reaction rate and the larger catalyst particle size were taken as the most critical condition [40], and the obtained data (Table S1, Supplementary Materials) indicated the absence of internal and external mass transfer limitations.

Figure 6A shows the global glycerol conversion (X_{Gly}) and conversion to gas (X_{Gas}), as well as hydrogen yield (Y_{H2}). The activity of NiAl/SBA-15 and NiAl-NCF was much lesser than the reference NiAl catalyst (X_{Gly} of 6% and 19%, respectively, vs 64% by NiAl). Accordingly, the former achieved a very low hydrogen yield, below 2%. Catalyst NiAl-

NCN showed higher activity (X_{Gly} = 80%; X_{Gas} = 40%) than the reference catalyst NiAl (X_{Gly}: 64%; X_{Gas}: 27%). Moreover, NiAl-NCN achieved the highest hydrogen yield (9.4%).

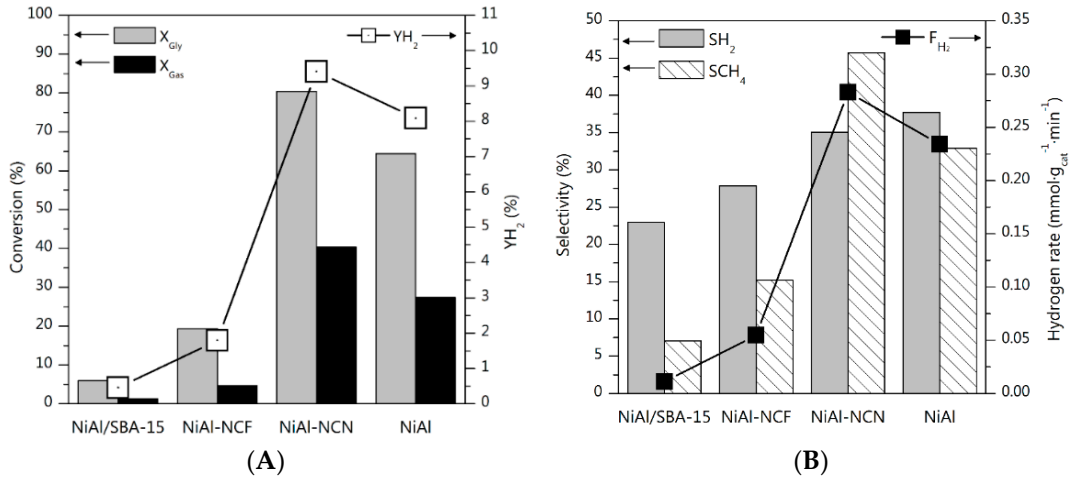

Figure 6. (**A**) Glycerol conversion, conversion to gas and hydrogen yield; (**B**) Selectivity to H_2 and CH_4, and H_2 production rate. Reaction conditions: 235 °C/35 bar, WHSV = 24.5 h^{-1}. Reaction time: 3 h TOS.

The superior performance of NiAl-NCN could be associated with its improved metallic Ni accessibility (Table 1) and its two-fold higher S_{BET}, with wormhole-like rods, which could facilitate the diffusion throughout the solid. The large Ni^0 domains and the low metallic nickel surface area could explain the poor performance of the NiAl-NCF catalyst. In the case of NiAl/SBA-15 catalyst, its limited activity could be associated with the encapsulation of Ni^0 inside the SBA-15 channels, hindering its availability for reactants. Moreover, NiAl/SBA-15 contained 50% larger Ni^0 crystallites than NiAl.

Table S2 (Supplementary Materials) shows a comparison between our NiAl and NiAl-NCN assays and other Ni catalysts reported in the literature).

2.2.1. Gas-Phase Products

Figure 6B depicts the selectivity of H_2 and CH_4. SH_2 increased in the following order: NiAl/SBA-15 < NiAl-NCF < NiAl-NCN < NiAl. Regarding the SCH_4, it was maximum for NiAl-NCN (i.e., 45.7% vs. 32.8% of NiAl). The less active catalysts presented SCH_4 values below 15.2%. These results evidenced H_2 consumption by side reactions, promoted by the high Ni^0 accessibility in NiAl-NCN catalyst, which contained the smallest metallic entities. NiAl-NCN achieved a 20% larger H_2 production rate than NiAl (0.28 vs. 0.23 $mmol_{H2}/g_{cat}{\cdot}min$). As a drawback, it had the highest SCH_4 (45.7%). An increase in the H_2 partial pressure inhibits the reforming reaction; hence, the H_2 was consumed in a side methanation reaction [41,42].

Characteristic properties of the gaseous stream are shown in Table 3. It can be observed that the selectivity to gas varied as follows: NiAl-NCN> NiAl> NiAl-NCF> NiAl/SBA-15, being ~50% lower for NiAl/SBA-15 and NiAl-NCF than for NiAl. NiAl-NCN catalyst enhanced the production of gaseous products (F_{Gas}) (i.e., 1.4 times that of reference NiAl). Finally, NiAl-NCF presented poor F_{Gas} and S_{Gas}, in line with its poor glycerol conversion.

Table 3. Gas-phase product analysis.

Catalyst	F_{Gas} (mmol/g_{cat}·min)	S_{Gas} (%)	Composition (vol.%)				H_2/CO_2	CO_2/CH_4
			H_2	CO_2	CO	CH_4		
NiAl	0.48	42	50.8	26.4	0.8	20.0	1.8	1.5
NiAl/SBA-15	0.01	21	77.5	6.6	3.3	8.8	12.9	0.6
NiAl-NCN	0.66	50	42.1	31.1	0.5	24.0	1.4	1.3
NiAl-NCF	0.09	24	65.0	18.1	2.0	12.0	3.6	1.2

H_2 was the most abundant gas product by all catalysts, followed by CO_2 and CH_4, which account for more than 97 vol.% of the reaction products. Other compounds such as CO and C2+ were found in much lesser concentrations. In contrast to the steam reforming of glycerol at atmospheric pressure, where CO and H_2 are the main products (CO/H_2 = 0.5) [41,43], in the aqueous-phase conversion, only trace amounts of CO (CO/H_2 < 0.04) were generated. This behavior could be associated with the lower temperature, which is beneficial for the WGS equilibrium [44]. NiAl produced a gaseous stream with a higher concentration in H_2 and lower in CH_4 as compared to NiAl-NCN, indicating that the improvement in H_2 yield for NiAl-NCN catalyst also favored methanation reaction, where the produced hydrogen is consumed. The gaseous stream from the less active catalysts was largely composed of H_2 (NiAl/SBA-15: 77.5%; NiAl-NCF: 65%). The H_2 production rate of both catalysts was 5-36 times lower than NiAl-NCN. Regarding the low concentration of CO in the gas stream for all the catalysts tested (<4.2%), it should be attributed to the effectiveness of nickel aluminate in catalyzing WGS reaction at the temperature and pressure conditions used in the APR [45,46].

The H_2/CO_2 ratio for NiAl/SBA-15 and NiAl-NCF catalysts (3.6−12.9 range) were notably higher than the stoichiometric reforming ratio (7/3); despite the low conversion attained by these catalysts, the obtained main product was still H_2. Contrarily, catalyst NiAl-NCN showed an H_2/CO_2 ratio lower than that of NiAl (1.4 vs. 1.8). Indeed, the CO_2/CH_4 for those samples suggested that H_2 was consumed in side reactions, such as CO hydrogenation (methanation).

2.2.2. Liquid-Phase Products

The fact that values of X_{gas} were lower than X_{Gly} for all the catalysts suggests that a significant fraction of the reacted carbon atoms were retained within the liquid phase products (Table 3: 50% for NiAl-NCN, 42% for NiAl). In view of the very poor performance of NiAl/SBA-15 and NiAl-NCF catalysts, the analysis of the liquid products was focused on the comparison of the two most active catalysts, i.e., reference NiAl and nanocasted NiAl-NCN. The composition (in glycerol-free base) of the liquid phase is shown in Figure 7.

A molar flow of liquid products of 0.52 $mmol_C/g_{cat}$·min was measured for catalyst NiAl-NCN (i.e., 12% higher than reference NiAl). The main liquid compound was 1,2-propyleneglycol (1,2-PG), followed by ethyleneglycol (EG) and ethanol (EtOH), accounting for over 80% of the liquid products. Methanol (MeOH), hydroxyacetone (HA), and acetaldehyde (MeCHO) were detected to a much lesser extent. There were no significant differences in the liquid product distribution between both catalysts.

In our previous work, considering the gas and liquid product distribution, we suggested a two-path reaction scheme for glycerol APR [18]. As depicted in Scheme 1, both the metallic and the acid function of the catalyst were involved. In a simple way, the acid function can be deemed essential for the dehydration reaction, while the metal function catalyzed both dehydrogenation/hydrogenation reactions [44]. Dehydrogenation of glycerol on metallic sites was the preferred pathway (Route A) for H_2 production by the APR of oxygenated compounds. Among the detected liquids, MeCHO, MeOH, EtOH, and EG corresponded to Route A path, while 1,2-PG and HA to Route B path.

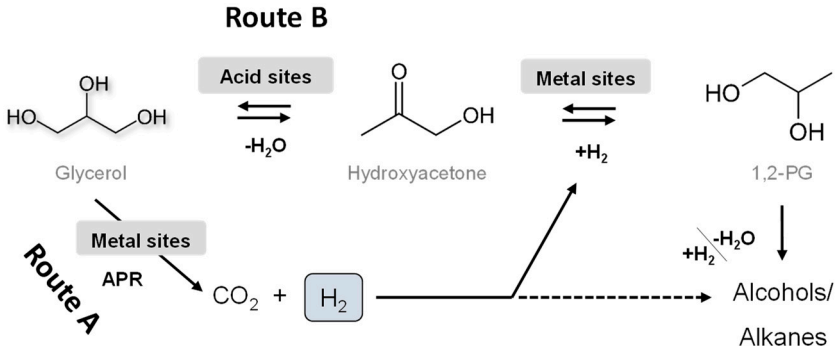

Scheme 1. Reaction path for the glycerol hydrodeoxygenation with in situ produced hydrogen.

Among the identified liquid products, those from Route A prevailed for both catalysts. The ratio Route A/Route B, as provided by the F_{Cliq}, was slightly higher for NiAl-NCN (0.79 vs. 0.68), despite its higher acid/base ratio (Table 1: 2.7 vs. 1.7). Indeed, the smaller metallic nickel entities of the nanocasted catalyst could promote the hydrogenation of the intermediate liquid compounds, such as hydroxyacetone (to propylene glycol) and acetaldehyde (to ethanol).

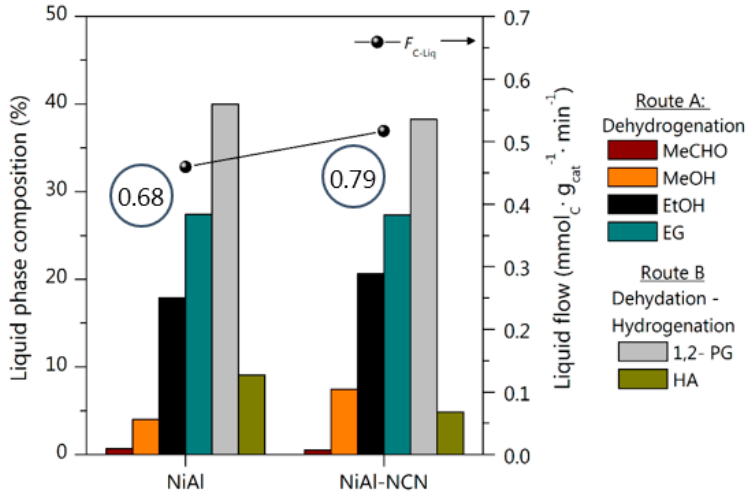

Figure 7. Molar composition of the main liquid products and total produced liquid flow. In circles: Route A/Route B product ratio. Reaction conditions: 235 °C/35 bar, WHSV = 24.5 h^{-1}. Reaction time: 3 h TOS.

2.2.3. Effect of Residence Time

The catalytic performance of NiAl-NCN and NiAl catalysts was evaluated for a wide range of residence time values (WHSV, on the basis of total flowrate, ranged 98-6 h^{-1}). Experiments were run at 235 °C/35 bar, with a feed of 10 wt.% glycerol–water solutions. The results obtained are shown in Figure 8.

The residence time of reactants showed a huge impact on the aqueous-phase transformation of glycerol for both catalysts. As could be expected, a longer residence time resulted in a higher glycerol conversion (Figure 8A). A similar outcome was reported by others [47,48]. Throughout all the investigated residence time ranges, NiAl-NCN catalyst was more active than NiAl (i.e., higher X_{Gly}). For instance, at 10 g_{cat}·h/mol_{gly}, NiAl-NCN achieved X_{Gly} = 35.5% (vs. 23.6% by NiAl). At the highest residence time of 158 g_{cat}·h/mol_{gly}, both catalysts converted a similar percentage of glycerol (99–98%). The glycerol conversion to gas also increased with residence time (not shown). This indicated that at higher residence time, the reforming of intermediate products was promoted; thus, more reforming end-products (CO_2 and H_2) were obtained [49]. NiAl-NCN showed a higher yield of hydrogen at those contact times.

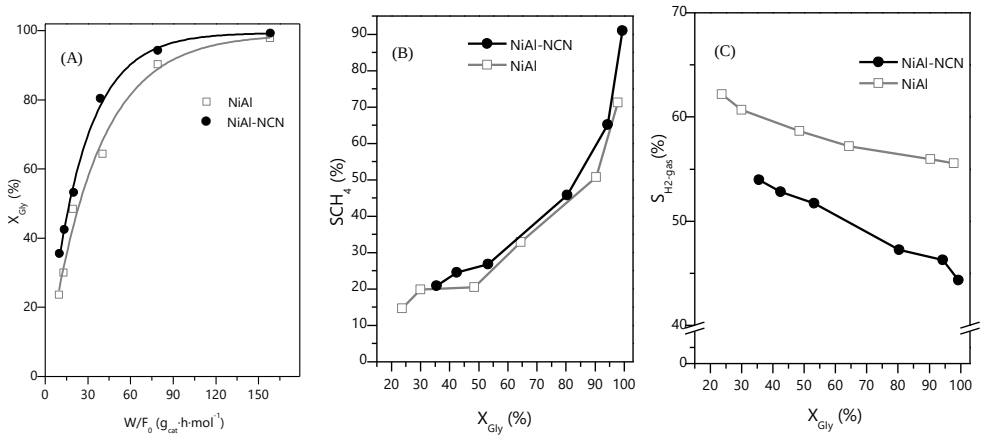

Figure 8. (**A**) Effect of the residence time on $X_{Gly;}$ (**B**) SCH_4 vs X_{Gly}; (**C**) $S_{H2\text{-}Gas}$ vs. X_{Gly}.

Although in the whole residence time range used catalyst NiAl-NCN presented higher X_{Gly}, the trend in YH2 was the opposite: YH2 of catalyst NiAl was higher than that of the nanocasted catalyst in the whole range (not shown). This behaviour could be associated with the high selectivity to CH4 shown by NiAl-NCN in the whole conversion range. (Figure 8B). The activity improvement led to the high availability of H_2, which simultaneously could favor the methanation reaction or others, such as hydrogenation, to produce liquid products (ethanol and 1,2-PG) [14].

In order to rationalize the results obtained for the selectivity to hydrogen, $SH_{2\text{-}gas}$ was calculated, considering the moles of H_2 produced with respect to hydrogen consumed in alkanes production (Figure 8C). Notably, NiAl-NCN showed lower values of $SH_{2\text{-}gas}$ in the whole reaction range, which agreed with its higher SCH_4. $SH_{2\text{-}gas}$ followed a decreasing trend with X_{Gly}, indicating more hydrogen was consumed in alkane formation as conversion increased. A similar trend was reported by others, suggesting that CO hydrogenation was lowered at short contact times [50].

2.3. Spent Catalysts Characterization

The main physico-chemical characteristics of exhausted catalysts are shown in Table 4. Interestingly, nanocasted catalysts suffered less nickel leaching than parent NiAl. Aluminum leaching was negligible for all catalysts, except for NiAl-NCF, which accounted for 1%. Results revealed that silica was also leached. In the case of NiAl/SBA-15 assay, it accounted for 5.5%. For the nanocasted catalysts, Si leaching increased to 31% and 94% for NiAl-NCF and NiAl-NCN, respectively, exaggerated by their low Si content.

Table 4. Physico-chemical properties of glycerol APR exhausted catalysts.

	Leaching (%)						
Catalyst	**Ni**	**Al**	**Si**	**ΔS_{BET}[a] (%)**	**New Phases (XRD)**	**Δd_{Ni^0}[a] (%)**	**Ni oxidized (%)**
NiAl	0.7	0.05	n.a.	+37	AlO(OH)	−9	60
NiAl/SBA-15	0.3	0.04	5.5	−42	$Ni_3Si_2O_5(OH)_4$	+18	67
NiAl-NCN	0.1	0.06	94	+33	$Ni(OH)_2{\cdot}0.75H_2O$	−6	60
NiAl-NCF	0.4	1.02	31	+137	n.d.	+30	44

[a] variation with respect to their fresh reduced form.

S_{BET} significantly decreased for the spent NiAl/SBA-15 (by 42%), indicative of the low textural stability of SBA-15 under hydrothermal conditions [51]. The incorporation of Ni-Al oxide and the high calcination temperature used did not seem to stabilize enough the siliceous material since structural collapse occurred under reaction conditions. The blockage of the access of reactants to the active sites due to the collapse of the pores could

explain the poor catalytic performance of this catalyst. On the contrary, S_{BET} of both nanocasted catalysts increased after reaction, as reference NiAl did, probably due to the re-deposition of leached aluminum as boehmite [52]. This fact also could explain the low leaching of aluminum.

The XRD patterns (Figure 9) of all the spent catalysts showed peaks from $NiAl_2O_4$, suggesting that the spinel phase was preserved. Moreover, intense XRD features of metallic Ni were still found for all the used catalysts, denoting that bulk metallic Ni nanoparticles were also preserved. Some new XRD peaks appeared, likely due to phase transformations under the hydrothermal conditions employed.

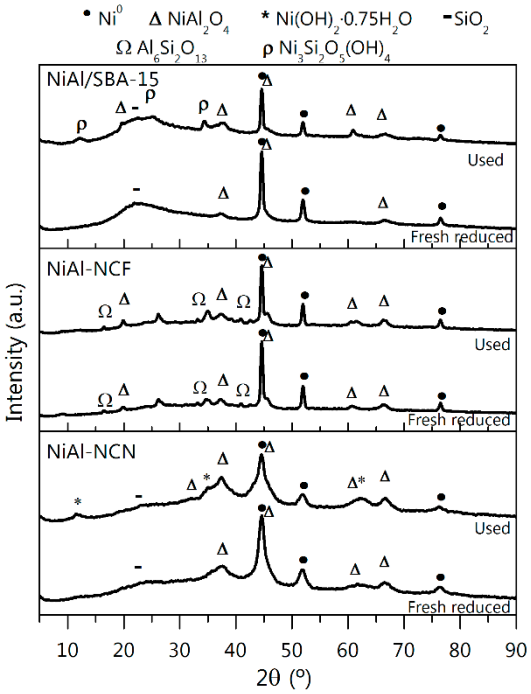

Figure 9. XRD of spent catalysts.

NiAl/SBA-15 showed peaks at 12.2°, 24.8°, and 34.4° 2θ, which could be assigned to the pecoraite phase ($Ni_3Si_2O_5(OH)_4$) (JCPDS 049-1859). This phase could be formed by hydroxylation reactions enhanced by the acidic aqueous medium. According to the mechanisms proposed by Park et al. [53], under hydrothermal conditions, Ni^0 can be oxidized to nickel hydroxide, which can diffuse into silica layers and react with surface hydroxyls, resulting in nickel phyllosilicate polymerization. This could explain the low nickel leaching by this solid. The loss of nickel in other phases is detrimental to the APR performance.

The diffraction pattern of the spent NiAl-NCF almost replicated that from the fresh reduced form, with the absence of new phases. XRD from spent NiAl-NCN showed new reflections at 12.2°, 35°, and 62.2° 2θ, corresponding to the formation of nickel hydroxide hydrate ($Ni(OH)_2{\cdot}0.75H_2O$) (JCPDS 038-0715). The nickel hydroxylation reaction was highly probable after the oxidation of Ni^0 at acid pH [54]. The absence of peaks from pecoraite in this assay could be due to the low amount of silica in this solid. It is noteworthy that diffraction peaks from boehmite were not detected by XRD, suggesting it was amorphous or existed as a small domain (XRD detection limit: 2 nm) [55]. The absence of carbon XRD signal indicated no coke formation. Operating at low temperature, as the aqueous-phase reforming does, would prevent the formation of carbonaceous deposits [28].

The crystallite size of Ni^0 (Table 4) varied differently after the reaction. Certain coalescence of Ni^0 occurred on NiAl/SBA-15 and NiAl-NCF exhausted catalyst (increase by 18–30%), while Ni^0 crystallites slightly shrugged for NiAl-NCN and NiAl catalysts (by 6–9%). The structural ordering accomplished in the NiAl-NCN catalyst could prevent Ni

sintering [26]. According to them, the large surface area and the additional mesopores of the wormhole-like rod structure (obtained by partial filling of the SBA-15 pores) can prevent the growth and aggregation of metal nanoparticles.

The spent catalysts were subjected to H_2-TPR analysis, and the obtained reduction profiles are presented in Figure S3 (Supplementary Materials). All the spent catalysts showed additional H_2 consumption compared to the $TPR_{700–950}$ profiles from the fresh reduced assays (Figure 5). They can be grouped into low-intermediate (110–700 °C) or high (>700 °C) temperature ranges. The high-temperature peak was related to the reduction of the Ni^{2+} in the spinel structure, and its position coincided with that of corresponding fresh reduced samples. The low-temperature peaks could be associated with the reduction of Ni^{2+} species and/or deposited organic liquid compounds.

In order to discern among different hydrogen uptake events at low-intermediate temperature, additional H_2-TPR coupled to MS experiments were carried out for catalysts NiAl-NCN and NiAl (Figure S4 Supplementary Materials). Release of CH_4 commenced at low-intermediate temperature (200–400 °C), which confirmed that the high-temperature peak corresponded to the reduction of Ni^{2+} in spinel. CH_4 was formed by the reduction of organic matter (unreacted glycerol and intermediate liquid products with low boiling point) adsorbed into the catalyst pores [56]. The H_2O peak in the 400–700 °C interval corresponded to the reduction of NiO. Assuming an uptake of two moles of H_2 per mol of CH_4 released, the percentage of nickel oxidized was estimated (Table 4). It was evidenced that Ni^0 could be readily oxidized during the aqueous-phase reaction. Indeed, it was recognized as one of the fundamental reasons for catalyst deactivation in aqueous-phase reactions [56]. Transition metals are thermodynamically prone to oxidation (which is the preliminary stage of leaching), and avoiding it is a challenge for the liquid phase reactions [57]. Since Ni^0 was detected by XRD in the exhausted catalysts, it could be deduced that oxidation of nickel was limited to the outermost layers of nickel particles. However, this event strongly diminishes the available metallic surface.

Among the nanocasted catalysts, NiAl-NCF was the one that better preserved nickel in its metallic form, with 44% of the nickel being oxidized. Interestingly, this catalyst had the lowest nickel metallic surface area, about five times lower than that of NiAl-NCN and NiAl. Contrarily, NiAl/SBA-15 catalyst suffered the most intense nickel oxidation (67% of Ni). The percentage of oxidized nickel in NiAl-NCN and the reference NiAl catalyst was similar, although the crystallite size was reduced by half in the former. It could be associated with the inhibition of oxidation due to a more favorable structural configuration, that is, nickel nanoparticles hidden in the wormhole-like rod structure.

To sum up, catalyst stability issues could be assigned to the effect of two facts, namely the oxidation of Ni^0 and transformations and the creation of new phases. The first fact has also been recognized by other authors as one of the main deactivation factors [58]. The effect of the deposition of carbonaceous materials seemed to be non-significant for these catalysts.

3. Materials and Methods

3.1. Catalysts Synthesis

The siliceous hard template SBA-15 was synthesized by hydrothermal polymerization of silica (at 110 °C and 4 bar for 24 h in a batch autoclave reactor) using an amphiphilic block copolymer (Pluronic, P123) as a structure directing agent, and tetraethyl orthosilicate (TEOS) as silica source. Both P123 and TEOS were purchased from Sigma-Aldrich The obtained suspension was filtered and rinsed with deionized water. Finally, the solid was dried at 110 °C for 18 h and then calcined at 850 °C for 6 h (heating rate 1 °C/min). The obtained solid was labeled as SBA-15.

Then, ethanolic solutions of nickel(II) nitrate tetrahydrate (Sigma-Aldrich) and aluminum(III) nitrate nonahydrate (Fluka) in a molar ratio 1:2 were used as metal precursors, being incorporated into the SBA-15 template by wetness co-impregnation method. The obtained solid was dried overnight at 70 °C and finally calcined at 850 °C for 4 h (heating

rate 1 °C/min). This composite was labeled NiAl/SBA-15 and was the precursor for the nanocasted solids.

Two methods were used for template removal. NiAl-NCN was obtained after treating the precursor with 2 M NaOH aqueous solution at 60 °C under constant stirring for 1 h, followed by drying at 110 °C for 24 h. NiAl-NCF was obtained by calcination at 650 °C for 4 h (heating rate 5 °C/min) of a solid mixture of precursor and Teflon with a sample:Teflon mass ratio of 2:9. The Teflon-assisted silica removal method avoids the use of toxic HF [21].

Bulk nickel aluminate spinel (NiAl) was selected as reference material. NiAl catalytic precursor was synthesized by basic coprecipitation (at pH 8) with Ni/Al = 0.5 mole ratio and calcined at 850 °C for 4 h (heating rate 10 °C/min). NiAl synthesis details could be found elsewhere [18].

3.2. Catalysts Characterization

The bulk chemical composition of the samples was analyzed by ICP-MS. The number of leached metals in the overall post-reaction liquid samples was measured by ICP-AES. Both analyses were carried out in the Advanced Research Facilities (SGIker) from the UPV/EHU. The textural properties of the catalysts were evaluated from N_2 adsorption-desorption isotherms at 77 K in a Micromeritics TriStar II 3020 equipment. Before the experiment, the solid was degassed at 300 °C for 10 h. The specific surface area and pore size distribution were determined by BET and BJH methods, respectively.

The crystalline properties of the samples were determined by means of a PANalytical Xpert PRO diffractometer with Cu kα radiation (λ = 1.542 Å) suitable to analyze polycrystalline solids. X-ray diffracted radiation was recorded each 2.5 s rotating the detector from 10° to 80° 2θ at 0.026° steps. The identification of the crystalline phases was carried out based on the ICDD database, and the crystallite sizes were estimated by Scherrer equation from the full width at half maximum (FWHM) value of the most intense peak.

Reducibility of the solids was evaluated by temperature-programmed reduction with hydrogen (H_2-TPR) performed in a Micromeritics AutoChem 2920 apparatus. The sample (about 70 mg) was flushed under 50 mL/min flow of He at 550 °C for 1 h prior to the test. Then, analysis was carried out by flowing 50 mL/min of 5% H_2/Ar stream through the sample and raising the temperature from room temperature to 950 °C at 10 °C/min, monitoring the signal by thermal conductivity detector (TCD). The water formed during the reduction was trapped using a cold trap. The total H_2-uptake was calculated from the integration of the H_2-TPR profile and defined as TPR_{950}.

Additional H_2-TPR runs were carried out with the aim of determining the fraction of reduced nickel and the Ni speciation. First, the sample was reduced at 700 °C for 1 h, simulating the reduction step conducted prior to the catalytic tests. Then, the sample was cooled down to room temperature in He flow, and afterward, the temperature was increased up to 950 °C. The H_2 consumption in this second step was defined as $TPR_{700–950}$. The degree of reduction (DR_{Ni}) was calculated as the fraction of the amount of H_2 consumed during the previous reduction step (TPR_{700}) with respect to the total amount of H_2 consumed during the full reduction (TPR_{950}). The TPR profiles were subjected to Gaussian deconvolution to estimate the content of the different nickel species as well. In order to estimate the percentage of oxidized nickel, TPR-MS experiments were performed with the same protocol as TPR_{950} but removing the water trap and analyzing the exhaust gases by Mass Spectrometer (Pffeifer Vacuum OmniStar) following the evolution of H_2, CH_4 and H_2O signals.

The morphology and particle size of the catalysts were measured by Transmission Electron Microscopy, with a TECNAI G2 20 TWIN microscope with LaB_6 filament at 200 kV. Additionally, this apparatus was equipped with an EDAX-EDS microanalysis system, allowing spot elemental analysis or chemical characterization. The mean diameter of the

metallic Ni particle was estimated from the volume to surface ratio as shown in Equation (1), and by measuring the diameter (d) of a large number of particles (>200 particles).

$$d_{Ni^0,TEM} = \frac{\sum_i n_i d_i^3}{\sum_i n_i d_i^2} \quad (2)$$

The nickel dispersion (D_{Ni°) was estimated applying d-FE model [59], as follows:

$$D_{Ni^0}(\%) = \frac{5.01 d_{at} \sum_j n_j d_j^2 + 2.64 d_{at}^{0.81} \sum_k n_k d_k^{2.19}}{\sum_i n_i d_i^3} \quad (3)$$

where d_i, d_j and d_k are the particles of "i", "j" and "k" diameter; n_i is the number of particles with diameter d_i, n_j is the number of particles with diameter d_j ($d_j > 24 d_{at}$), n_k is the number of particles with diameter d_k ($d_k \leq 24 d_{at}$), and d_{at} is the atomic diameter of metallic nickel (0.248 nm).

The metallic nickel surface area (S_{Ni°) was calculated as follows:

$$S_{Ni^0}\,(m^2/g) = \frac{A_{at} \times C_{Ni} \times D_{Ni^0} \times N_A}{MW_{Ni}} \quad (4)$$

where, A_{at} is the atomic area of Ni, N_A is the Avogadro number, MW_{Ni} is the molecular weight of Ni, and C_{Ni} is the exuded nickel content.

The density of acid and basic sites was determined by NH_3, and CO_2 temperature programmed desorption, respectively, in a Micromeritics AutoChem 2920 equipment. Prior to the analysis, the sample (60 mg) was degassed with He at 550 °C for 1 h to remove adsorbed CO_2 and H_2O and cooled down to room temperature. Subsequently, the catalyst was reduced with 5% H_2/Ar (50 mL/min) at 700 °C for 1 h, and again cooled down to room temperature under He flow. For acidity evaluation, a series of 10% NH_3/He pulses (loop volume 0.5 mL) were injected at 90 °C until saturation of the sample, flushing with He flow in between each ammonia pulse. After that, the sample was heated under He up to 850 °C at 10 °C/min rate. Desorbed NH_3 was measured by TCD detector. For basicity analysis, the sample was exposed to 50 mL/min 5% CO_2/He at 50 °C for 1 h (enough for saturation) and subsequently flushed out with He flow for additional 1 h with the aim of removing physisorbed CO_2. Finally, the temperature was raised to 850 °C at 10 °C/min, and the desorbed CO_2 was measured by MS spectrometer (Pffeifer Vacuum OmniStar).

FTIR was recorded on a Cary 600 Series FTIR apparatus with the catalyst powder diluted in a KBr pellet in the 500–4000 cm^{-1} region with a resolution of 4 cm^{-1}.

3.3. Catalytic Performance Evaluation

Glycerol reforming was carried out for an aqueous solution of 10 wt.% glycerol. The reactions were carried out in a fixed bed reactor operating at WHSV = 24.5 h^{-1} (determined as the ratio between total feed mass-flowrate and mass of fresh catalyst). Catalysts were in situ reduced at 700 °C for 1 h, heating at 5 °C/min, in 20%H_2/Ar flow. The reaction was carried out at 235 °C and 35 bar. Reaction products were passed through a liquid/gas separator placed at the reactor outlet. The gaseous products were analyzed by an Agilent 490 Micro GC, and the liquid products by either GC and HPLC chromatography FID (Agilent 6890 N) and HPLC-RI (Waters, Hi-Plex H column). Total Organic Carbon (TOC) was measured for liquid samples on a Shimadzu TOC-L apparatus. The carbon balance accounted for about 93–104%. Standard deviation in X_{Gly} values measured in duplicate experiments was below 5%.

The criteria for mass transfer limitations were estimated through the Weisz–Prater criterion Φ_{WP} and the Mears criterion MR. Φ_{WP} and MR results confirmed the absence of

internal and external mass diffusion effects, which can affect the activity results (Table S2, Supplementary Materials).

Glycerol conversion (X_{Gly}) was evaluated from the inlet and outlet molar flow of glycerol:

$$X_{Gly}(\%) = 100 \times \frac{F^0_{Gly} - F_{Gly}}{F^0_{Gly}} \quad (5)$$

Conversion to gas (X_{Gas}) was evaluated from the carbon moles in the feedstream and the liquid products.

$$X_{Gas}(\%) = 100 \times \frac{F^0 - F_C^{liquid}}{F^0_C} \quad (6)$$

H_2 yield (Y_{H2}) was defined as follows:

$$Y_{H2}(\%) = 100 \times \frac{FH_2}{F_{Gly}{}^0} \times \frac{1}{7} \quad (7)$$

where F_{H2} is the molar flow of H_2. Selectivity to gas (S_{Gas}) was calculated as:

$$S_{Gas}(\%) = 100 \times \frac{\sum_n F_{Gas-n} \times C_{at,n}}{F^0_{Gly} - F_{Gly}} \times \frac{1}{3} \quad (8)$$

where $F_{Gas\text{-}n}$ is the molar flow of the n compound ($mmol_C/min$); and $C_{at,n}$ are the number of carbons in the n compound. Selectivity to hydrogen (S_{H2}) and Selectivity to hydrogen in the gas phase ($S_{H2\text{-}gas}$) were calculated as follows:

$$S_{H2}(\%) = 100 \times \frac{FH_2}{F^0_{Gly} - F_{Gly}} \times \frac{3}{7} \quad (9)$$

$$S_{H2-gas}(\%) = 100 \times \frac{FH_2}{F_{H_2} + \sum (n+1) \cdot F_{C_nH_{2n+2}}} \quad (10)$$

Selectivity to CH4 (S_{CH4}) was defined as follows:

$$S_{CH4}(\%) = 100 \times \frac{FCH_4}{F^0_{Gly} - F_{Gly}} \quad (11)$$

All the reaction indices above were obtained at TOS = 3 h.

4. Conclusions

The physicochemical and the catalytic properties of the nickel aluminate spinels synthesized by the nanocasting technique were highly influenced by the template removal method. NiAl/SBA-15 solid, which preserved the siliceous template, had a higher Ni/Al ratio than the nominal and very high surface area. However, its reducibility deteriorated, and the acid/basic site ratio increased with respect to NiAl. NaOH-etched NiAl-NCN solid showed improved textural characteristics, with smaller metallic nickel particles and improved Ni^0 dispersion, with a similar acid/basic site density ratio to NiAl. The ordering accomplished by nanocasting synthesis provided a wormhole-like rod structure that could facilitate the diffusion of reagents throughout the catalyst pores. Teflon-assisted template removal led to a solid with deteriorated textural and metallic nickel dispersion characteristics, which increased the acid/basic sites ratio.

Both NiAl/SBA-15 and NiAl-NCF catalysts showed very poor catalytic performance for the glycerol transformation, with less than 20% glycerol converted. NiAl-NCN catalyst presented improved activity with respect to NiAl, with a 20% higher hydrogen production rate but, as a drawback, higher methane formation. Such a performance was attributed

to its smaller and better dispersed Ni^0 particles. There were no relevant differences in the chemical route followed by NiAl and NiAl-NCN catalysts in the glycerol aqueous-phase conversion since the composition of the liquid phase remained similar. Route A/Route B liquid products were slightly favored by the nanocasted NiAl-NCN catalyst.

The analysis of the glycerol conversion at various spatial times indicated that the nanocasting synthesis could improve the conversion of glycerol and conversion to gas. Those are accompanied by increased hydrogenation of carbon oxides (methanation), to the detriment of the yield and selectivity to H_2.

Moreover, obtained results demonstrated that the nanocasted catalyst etched by NaOH showed promising stability, though changes in the oxidation state of nickel are still a challenge to be addressed. It efficiently stabilized the active phase and prevented sintering. In turn, other deactivation causes extensively reported for APR, such as leaching or phase transitions related to alumina, could contribute to lesser stability.

Supplementary Materials: The following supporting information can be downloaded at: https://www.mdpi.com/article/10.3390/catal12060668/s1, Figure S1. FTIR of SBA-15 calcined at 850 °C; Figure S2. Variation of reaction indices with TOS; Figure S3. Reduction profiles of used catalysts in aqueous-phase reaction for 3 h; Figure S4. TPR-MS of used catalysts in aqueous-phase reaction for 3 h; Table S1. Parameters of mass transfer limitations for supported (NiAl/SBA-15) and nanocasted catalysts; Table S2. Comparison with other works in the literature [60–66].

Author Contributions: Investigation and writing—original draft preparation, A.M.-M.; Methodology and writing—review and editing, U.I.-V.; Resources, funding acquisition and supervision, M.Á.G.-O.; Conceptualization, writing—review and editing, funding acquisition, J.L.A. All authors have read and agreed to the published version of the manuscript.

Funding: This research was supported by grant PID2019-106692EB-I00 funded by MCIN/AEI/10.13039/501100011033.

Acknowledgments: The authors are thankful for technical support provided by SGIker of UPV/EHU and European funding (ERDF and ESF).

Conflicts of Interest: The authors declare no conflict of interest.

References

1. Chen, D.; Rojas, M.; Samset, B.H.; Cobb, K.; Diongue Niang, A.; Edwards, P.; Emori, S.; Faria, S.H.; Hawkins, E.; Hope, P.; et al. Framing, Context, and Methods. In *Climate Change 2021: The Physical Science Basis*; Contribution of Working Group I to the Sixth Assessment Report of the Intergovernmental Panel on Climate Change; Cambridge University Press: Cambridge, UK; New York, NY, USA, 2021; pp. 147–286.
2. Touma, D.; Stevenson, S.; Lehner, F.; Coats, S. Human-driven greenhouse gas and aerosol emissions cause distinct regional impacts on extreme fire weather. *Nat. Commun.* **2021**, *12*, 212. [CrossRef] [PubMed]
3. Pachauri, R.K.; Allen, M.R.; Barros, V.R.; Broome, J.; Cramer, W.; Christ, R.; Church, J.A.; Clarke, L.; Dahe, Q.; Dasgupta, P.; et al. *Climate Change 2014: Synthesis Report*; Contribution of Working Groups I, II and III to the Fifth Assessment Report of the Intergovernmental Panel on Climate Change; IPCC: Geneva, Switzerland, 2014; 151p.
4. IEA Net Zero by 2050. IEA 2021. Available online: https://www.iea.org/reports/net-zero-by-2050 (accessed on 26 May 2022).
5. Checa, M.; Nogales-Delgado, S.; Montes, V.; Encinar, J.M. Recent advances in glycerol catalytic valorization: A review. *Catalysts* **2020**, *10*, 1279. [CrossRef]
6. Cortright, R.D.; Davda, R.R.; Dumesic, J.A. Hydrogen from catalytic reforming of biomass-derived hydrocarbons in liquid water. *Nature* **2002**, *418*, 964–967. [CrossRef]
7. Chheda, J.N.; Huber, G.W.; Dumesic, J.A. Liquid-phase catalytic processing of biomass-derived oxygenated hydrocarbons to fuels and chemicals. *Angew. Chem. Int. Ed.* **2007**, *46*, 7164–7183. [CrossRef]
8. Coronado, I.; Stekrova, M.; Reinikainen, M.; Simell, P.; Lefferts, L.; Lehtonen, J. A review of catalytic aqueous-phase reforming of oxygenated hydrocarbons derived from biorefinery water fractions. *Int. J. Hydrogen Energy* **2016**, *41*, 11003–11032. [CrossRef]
9. Meryemoglu, B.; Kaya, B.; Irmak, S.; Hesenov, A.; Erbatur, O. Comparison of batch aqueous-phase reforming of glycerol and lignocellulosic biomass hydrolysate. *Fuel* **2012**, *97*, 241–244. [CrossRef]
10. Remón, J.; Ruiz, J.; Oliva, M.; García, L.; Arauzo, J. Cheese whey valorisation: Production of valuable gaseous and liquid chemicals from lactose by aqueous phase reforming. *Energy Convers. Manag.* **2016**, *124*, 453–469. [CrossRef]
11. Coronado, I.; Arandia, A.; Reinikainen, M.; Karinen, R.; Puurunen, R.L.; Lehtonen, J. Kinetic Modelling of the Aqueous-Phase Reforming of Fischer-Tropsch Water over Ceria-Zirconia Supported Nickel-Copper Catalyst. *Catalysts* **2019**, *9*, 936. [CrossRef]

12. Pendem, C.; Sarkar, B.; Siddiqui, N.; Sivakumar Konathala, N.L.; Baskar, C.; Bal, R. K-Promoted Pt-Hydrotalcite Catalyst for Production of H2 by Aqueous Phase Reforming of Glycerol. *ACS Sustain. Chem. Eng.* **2018**, *6*, 2122–2131. [CrossRef]
13. Zoppi, G.; Pipitone, G.; Pirone, R.; Bensaid, S. Aqueous phase reforming process for the valorization of wastewater streams: Application to different industrial scenarios. *Catal. Today* **2022**, *387*, 224–236. [CrossRef]
14. El Doukkali, M.; Iriondo, A.; Gandarias, I. Enhanced catalytic upgrading of glycerol into high value-added H_2 and propanediols: Recent developments and future perspectives. *Mol. Catal.* **2020**, *490*, 110928. [CrossRef]
15. Davda, R.R.; Shabaker, J.W.; Huber, G.W.; Cortright, R.D.; Dumesic, J.A. A review of catalytic issues and process conditions for renewable hydrogen and alkanes by aqueous-phase reforming of oxygenated hydrocarbons over supported metal catalysts. *Appl. Catal. B Environ.* **2005**, *56*, 171–186. [CrossRef]
16. Pipitone, G.; Zoppi, G.; Pirone, R.; Bensaid, S. A critical review on catalyst design for aqueous phase reforming. *Int. J. Hydrogen Energy* **2022**, *47*, 151–180. [CrossRef]
17. Fasolini, A.; Cespi, D.; Tabanelli, T.; Cucciniello, R.; Cavani, F. Hydrogen from Renewables: A Case Study of Glycerol Reforming. *Catalysts* **2019**, *9*, 722. [CrossRef]
18. Morales-Marín, A.; Ayastuy, J.L.; Iriarte-Velasco, U.; Gutiérrez-Ortiz, M.A. Nickel aluminate spinel-derived catalysts for the aqueous phase reforming of glycerol: Effect of reduction temperature. *Appl. Catal. B Environ.* **2019**, *244*, 931–945. [CrossRef]
19. Huber, G.W.; Shabaker, J.W.; Dumseic, J.A. Raney Ni-Sn Catalyst for H_2 Production from Biomass-Derived Hydrocarbons. *Science* **2003**, *300*, 2075–2077. [CrossRef]
20. Zhu, J.; Gao, Q. Mesoporous MCo_2O_4 (M = Cu, Mn and Ni) spinels: Structural replication, characterization and catalytic application in CO oxidation. *Microporous Mesoporous Mater.* **2009**, *124*, 144–152. [CrossRef]
21. Singh, D.K.; Krishna, K.S.; Harish, S.; Sampath, S.; Eswaramoorthy, M. No More HF: Teflon-assisted ultrafast removal of silica to generate high-surface-area mesostructured carbon for enhanced CO_2 capture and supercapacitor performance. *Angew. Chem. Int. Ed.* **2016**, *55*, 2032–2036. [CrossRef]
22. De Sousa, F.F.; de Sousa Helvio, S.A.; Oliveira, A.C.; Junior, M.C.C.; Ayala, A.P.; Barros, E.B.; Viana, B.C.; Filho, J.M.; Oliveira, A.C. Nanostructured Ni-containing spinel oxides for the dry reforming of methane: Effect of the presence of cobalt and nickel on the deactivation behaviour of catalysts. *Int. J. Hydrogen Energy* **2012**, *37*, 3201–3212. [CrossRef]
23. Karam, L.; Reboul, J.; El Hassan, N.; Nelayah, J.; Massiani, P. Nanostructured nickel aluminate as a key intermediate for the production of highly dispersed and stable nickel nanoparticles supported within mesoporous alumina for dry reforming of methane. *Molecules* **2019**, *24*, 4107. [CrossRef]
24. Gil, A.G.; Wu, Z.; Chadwick, D.; Li, K. Ni/SBA-15 Catalysts for combined steam methane reforming and water gas shift—Prepared for use in catalytic membrane reactors. *Appl. Catal. A Gen.* **2015**, *506*, 188–196.
25. Carrero, A.; Calles, J.A.; García-Moreno, L.; Vizcaíno, A.J. Production of renewable hydrogen from glycerol steam reforming over bimetallic Ni-(Cu,Co,Cr) catalysts supported on SBA-15 silica. *Catalysts* **2017**, *7*, 55. [CrossRef]
26. Kim, H.; Kim, T.; Park, H.J.; Jeong, K.; Chae, H.; Jeong, S.; Lee, C.; Kim, C. Hydrogen production via the aqueous phase reforming of ethylene glycol over platinum-supported ordered mesoporous carbon catalysts: Effect of structure and framework-configuration. *Int. J. Hydrogen Energy* **2012**, *37*, 12187–12197. [CrossRef]
27. Al-Salihi, S.; Abrokwah, R.; Dade, W.; Deshmane, V.; Hossain, T.; Kuila, D. Renewable hydrogen from glycerol steam reforming using Co–Ni–MgO based SBA-15 nanocatalysts. *Int. J. Hydrogen Energy* **2020**, *45*, 14183–14198. [CrossRef]
28. Calles, J.A.; Carrero, A.; Vizcaíno, A.J.; García-Moreno, L. Hydrogen production by glycerol steam reforming over SBA-15-supported nickel catalysts: Effect of alkaline earth promoters on activity and stability. *Catal. Today* **2014**, *227*, 198–206. [CrossRef]
29. Azof, F.I.; Yang, Y.; Panias, D.; Kolbeinsen, L.; Safarian, J. Leaching characteristics and mechanism of the synthetic calcium-aluminate slags for alumina recovery. *Hydrometallurgy* **2019**, *185*, 273–290. [CrossRef]
30. Galarneau, A.; Desplantier, D.; Dutartre, R.; Di Renzo, F. Micelle-templated silicates as a test bed for methods of mesopore size evaluation. *Microporous Mesoporous Mater.* **1999**, *27*, 297–308. [CrossRef]
31. Remón, J.; Giménez, J.R.; Valiente, A.; García, L.; Arauzo, J. Production of gaseous and liquid chemicals by aqueous phase reforming of crude glycerol: Influence of operating conditions on the process. *Energy Convers. Manag.* **2016**, *110*, 90–112. [CrossRef]
32. Estevez, R.; Lopez-Pedrajas, S.; Blanco-Bonilla, F.; Luna, D.; Bautista, F.M. Production of acrolein from glycerol in liquid phase on heterogeneous catalysts. *Chem. Eng. J.* **2015**, *282*, 179–186. [CrossRef]
33. Jeon, S.; Roh, H.; Ju Moon, D.; Wook Bae, J. Aqueous phase reforming and hydrodeoxygenation of ethylene glycol on Pt/SiO_2-Al_2O_3: Effects of surface acidity on product distribution. *RSC Adv.* **2016**, *6*, 68433–68444. [CrossRef]
34. Guo, G.; Usman, M.; Liu, X.; Wang, Y.; Lu, G. Effect of support's basic properties on hydrogen production in aqueous-phase reforming of glycerol and correlation between WGS and APR. *Appl. Energy* **2012**, *92*, 218–223. [CrossRef]
35. Ghosh, B.K.; Hazra, S.; Naik, B.; Ghosh, N.N. Preparation of Cu nanoparticle loaded SBA-15 and their excellent catalytic activity in reduction of variety of dyes. *Powder Technol.* **2015**, *269*, 371–378. [CrossRef]
36. Zhao, D.; Feng, J.; Huo, Q.; Melosh, N.; Fredrickson, G.H.; Chmelka, B.F.; Stucky, G.D. Triblock copolymer syntheses of mesoporous silica with periodic 50 to 300 angstrom pores. *Science* **1998**, *279*, 548–552. [CrossRef] [PubMed]
37. Song, K.H.; Jeong, S.K.; Jeong, B.H.; Lee, K.-Y.; Kim, H.J. Effect of the Ni/Al Ratio on the Performance of $NiAl_2O_4$ Spinel-Based Catalysts for Supercritical Methylcyclohexane Catalytic Cracking. *Catalysts* **2021**, *11*, 323. [CrossRef]

38. Zhou, L.; Li, L.; Wei, N.; Li, J.; Basset, J.-M. Effect of $NiAl_2O_4$ Formation on Ni/Al_2O_3 Stability during Dry Reforming of Methane. *ChemCatChem* **2015**, *7*, 2508–2516. [CrossRef]
39. Li, G.; Hu, L.; Hill, J.M. Comparison of reducibility and stability of alumina-supported Ni catalysts prepared by impregnation and co-precipitation. *Appl. Catal. A Gen.* **2006**, *301*, 16–24. [CrossRef]
40. Godina, L.I.; Kirilin, A.V.; Tokarev, A.V.; Simakova, I.L.; Murzin, D.Y. Sibunit-Supported Mono- and Bimetallic Catalysts Used in Aqueous-Phase Reforming of Xylitol. *Ind. Eng. Chem. Res.* **2018**, *57*, 2050–2067. [CrossRef]
41. Dietrich, P.J.; Lobo-Lapidus, R.J.; Wu, T.; Sumer, A.; Akatay, M.C.; Fingland, B.R.; Guo, N.; Dumesic, J.A.; Marshall, C.L.; Stach, E.; et al. Aqueous phase glycerol reforming by PtMo bimetallic nano-particle catalyst: Product selectivity and structural characterization. *Top. Catal.* **2012**, *55*, 53–69. [CrossRef]
42. Seretis, A.; Tsiakaras, P. Aqueous phase reforming (APR) of glycerol over platinum supported on Al_2O_3 catalyst. *Renew. Energy* **2016**, *85*, 1116–1126. [CrossRef]
43. Iriondo, A.; Cambra, J.F.; Güemez, M.B.; Barrio, V.L.; Requies, J.; Sánchez-Sánchez, M.C.; Navarro, R.M. Effect of ZrO_2 addition on Ni/Al_2O_3 catalyst to produce H_2 from glycerol. *Int. J. Hydrogen Energy* **2012**, *37*, 7084–7093. [CrossRef]
44. Vaidya, P.D.; Lopez-Sanchez, J.A. Review of Hydrogen Production by Catalytic Aqueous-Phase Reforming. *ChemistrySelect* **2017**, *2*, 6563–6576. [CrossRef]
45. Morales-Marín, A.; Ayastuy, J.L.; Iriarte-Velasco, U.; Gutiérrez-Ortiz, M.A. Biohydrogen production by glycerol Aqueous-Phase Reforming: Effect of promoters (Ce or Mg) in the $NiAl_2O_4$ spinel-derived catalysts. *J. Environ. Chem. Eng.* **2021**, *9*, 106433. [CrossRef]
46. Li, D.; Li, Y.; Liu, X.; Guo, Y.; Pao, C.-W.; Chen, J.-L.; Hu, Y.; Wang, Y. $NiAl_2O_4$ Spinel Supported Pt Catalyst: High Performance and Origin in Aqueous-Phase Reforming of Methanol. *ACS Catal.* **2019**, *9*, 9671–9682. [CrossRef]
47. García, L.; Valiente, A.; Oliva, M.; Ruiz, J.; Arauzo, J. Influence of operating variables on the aqueous-phase reforming of glycerol over a Ni/Al coprecipitated catalyst. *Int. J. Hydrogen Energy* **2018**, *43*, 20392–20407. [CrossRef]
48. Kirilin, A.V.; Tokarev, A.V.; Murzina, E.V.; Kustov, L.M.; Mikkola, J.-P.; Murzin, D.Y. Reaction products and transformations of intermediates in the aqueous-phase reforming of sorbitol. *ChemSusChem* **2010**, *3*, 708–718. [CrossRef] [PubMed]
49. Kim, H.; Park, H.J.; Kim, T.; Jeong, K.; Chae, H.; Jeong, S.; Lee, C.; Kim, C. The effect of support and reaction conditions on aqueous phase reforming of polyol over supported Pt–Re bimetallic catalysts. *Catal. Today* **2012**, *185*, 73–80. [CrossRef]
50. He, Z.; Wang, X.; Gao, S.; Xiao, T. Effect of reaction variables on CO methanation process over $NiO–La_2O_3–MgO/Al_2O_3$ catalyst for coal to synthetic natural gas. *Appl. Petrochem. Res.* **2015**, *5*, 413–417. [CrossRef]
51. Nichele, V.; Signoretto, M.; Menegazzo, F.; Gallo, A.; Dal Santo, V.; Cruciani, G.; Cerrato, G. Glycerol steam reforming for hydrogen production: Design of Ni supported catalysts. *Appl. Catal. B Environ.* **2012**, *111–112*, 225–232. [CrossRef]
52. De Vlieger, D.J.M.; Mojet, B.L.; Lefferts, L.; Seshan, K. Aqueous Phase Reforming of ethylene glycol—Role of intermediates in catalyst performance. *J. Catal.* **2012**, *292*, 239–245. [CrossRef]
53. Park, J.C.; Lee, H.J.; Bang, J.U.; Park, K.H.; Song, H. Chemical transformation and morphology change of nickel-silica hybrid nanostructures via nickel phyllosilicates. *Chem. Commun.* **2009**, *47*, 7345–7347. [CrossRef]
54. Van Haasterecht, T.; Ludding, C.C.I.; de Jong, K.P.; Bitter, J.H. Toward stable nickel catalysts for aqueous phase reforming of biomass-derived feedstock under reducing and alkaline conditions. *J. Catal.* **2014**, *319*, 27–35. [CrossRef]
55. Melero, J.A.; Calleja, G.; Martínez, F.; Molina, R. Nanocomposite of crystalline Fe_2O_3 and CuO particles and mesostructured SBA-15 silica as an active catalyst for wet peroxide oxidation processes. *Catal. Commun.* **2006**, *7*, 478–483. [CrossRef]
56. El Doukkali, M.; Iriondo, A.; Cambra, J.F.; Gandarias, I.; Jalowiecki-Duhamel, L.; Dumeignil, F.; Arias, P.L. Deactivation study of the Pt and/or Ni-based γ-Al_2O_3 catalysts used in the aqueous phase reforming of glycerol for H_2 production. *Appl. Catal. A Gen.* **2014**, *472*, 80–91. [CrossRef]
57. Sievers, C.; Scott, S.L.; Noda, Y.; Qi, L.; Albuquerque, E.M.; Rioux, R.M. Phenomena affecting catalytic reactions at solid−Liquid interfaces. *ACS Catal.* **2016**, *6*, 8286–8307. [CrossRef]
58. Van Haasterecht, T.; Swart, M.; De Jong, K.P.; Bitter, J.H. Effect of initial nickel particle size on stability of nickel catalysts for aqueous phase reforming. *J. Energy Chem.* **2016**, *25*, 289–296. [CrossRef]
59. Borodziński, A.; Bonarowska, M. Relation between crystallite size and dispersion on supported metal catalysts. *Langmuir* **1997**, *13*, 5613–5620. [CrossRef]
60. Bastan, F.; Kazemeini, M.; Larimi, A.; Maleki, H. Production of renewable hydrogen through aqueous-phase reforming of glycerol over $Ni/Al_2O_3–MgO$ nano-catalyst. *Int J. Hydrogen Energy* **2018**, *43*, 614–621. [CrossRef]
61. El Doukkali, M.; Iriondo, A.; Arias, P.L.; Requies, J.; Gandarías, I.; Jalowiecki-Duhamel, L.; Dumeignil, F. A comparison of sol-gel and impregnated Pt or/and Ni based γ-alumina catalysts for bioglycerol aqueous phase reforming. *Appl. Catal. B Environ.* **2012**, *125*, 516–529. [CrossRef]
62. Park, Y.H.; Kim, J.Y.; Moon, D.J.; Park, N.C.; Kim, Y.C. Effect of $LaAlO_3$-supported modified Ni-based catalysts on aqueous phase reforming of glycerol. *Res. Chem. Intermed* **2015**, *41*, 9603–9614. [CrossRef]
63. Rahman, M.M.; Church, T.L.; Variava, M.F.; Harris, A.T.; Minett, A.I. Bimetallic Pt-Ni composites on ceria-doped alumina supports as catalysts in the aqueous-phase reforming of glycerol. *RSC Adv.* **2014**, *4*, 18951–18960. [CrossRef]
64. Manfro, R.L.; Pires, T.P.M.D.; Ribeiro, N.F.P.; Souza, M.M.V.M. Aqueous-phase reforming of glycerol using Ni-Cu catalysts prepared from hydrotalcite-like precursors. *Catal. Sci. Technolog.* **2013**, *3*, 1278–1287. [CrossRef]

65. Rahman, M.M. Aqueous-Phase Reforming of Glycerol over Carbon-Nanotube-Supported Catalysts. *Catal Lett.* **2020**, *150*, 2674–2687. [CrossRef]
66. Bastan, F.; Kazemeini, M.; Larimi, A.S. Aqueous-phase reforming of glycerol for production of alkanes over $Ni/Ce_xZr_{1-x}O_2$ nano-catalyst: Effects of the support's composition. *Renew. Energy* **2017**, *108*, 417–424. [CrossRef]